The Astrophysical Journal, 965:122 (13pp), 2024 April 20 https://doi.org/10.3847/1538-4357/ad2bfd
© 2024. The Author(s). Published by the American Astronomical Society.
OPEN ACCESS

Model-independent Approach of the JUNO ^{8}B Solar Neutrino Program

Jie Zhao[1], Baobiao Yue[2], Haoqi Lu[1], Yufeng Li[1], Jiajie Ling[2], Zeyuan Yu[1], Angel Abusleme[3,4], Thomas Adam[5], Shakeel Ahmad[6], Rizwan Ahmed[6], Sebastiano Aiello[7], Muhammad Akram[6], Abid Aleem[6], Tsagkarakis Alexandros[8], Fengpeng An[9], Qi An[10], Giuseppe Andronico[7], Nikolay Anfimov[11], Vito Antonelli[12], Tatiana Antoshkina[11], Burin Asavapibhop[13], João Pedro Athayde Marcondes de André[5], Didier Auguste[14], Weidong Bai[2], Nikita Balashov[11], Wander Baldini[15], Andrea Barresi[16], Davide Basilico[12], Eric Baussan[5], Marco Bellato[17], Antonio Bergnoli[17], Thilo Birkenfeld[8], Sylvie Blin[14], David Blum[18], Simon Blyth[1], Anastasia Bolshakova[11], Mathieu Bongrand[19], Clément Bordereau[20,21], Dominique Breton[14], Augusto Brigatti[12], Riccardo Brugnera[22], Riccardo Bruno[7], Antonio Budano[23], Jose Busto[24], Ilya Butorov[11], Anatael Cabrera[14], Barbara Caccianiga[12], Hao Cai[25], Xiao Cai[1], Yanke Cai[1], Zhiyan Cai[1], Riccardo Callegari[22], Antonio Cammi[26], Agustin Campeny[3], Chuanya Cao[1], Guofu Cao[1], Jun Cao[1], Rossella Caruso[7], Cédric Cerna[20], Chi Chan[27], Jinfan Chang[1], Yun Chang[28], Guoming Chen[29], Pingping Chen[30], Po-An Chen[21], Shaomin Chen[31], Xurong Chen[32], Yixue Chen[33], Yu Chen[2], Zhiyuan Chen[1], Zikang Chen[2], Jie Cheng[33], Yaping Cheng[34], Alexander Chepurnov[35], Alexey Chetverikov[11], Davide Chiesa[16], Pietro Chimenti[36], Artem Chukanov[11], Gérard Claverie[20], Catia Clementi[37], Barbara Clerbaux[38], Marta Colomer Molla[38], Selma Conforti Di Lorenzo[20], Daniele Corti[17], Flavio Dal Corso[17], Olivia Dalager[39], Christophe De La Taille[20], Zhi Deng[31], Ziyan Deng[1], Wilfried Depnering[40], Marco Diaz[3], Xuefeng Ding[12], Yayun Ding[1], Bayu Dirgantara[41], Sergey Dmitrievsky[11], Tadeas Dohnal[42], Dmitry Dolzhikov[11], Georgy Donchenko[35], Jianmeng Dong[31], Evgeny Doroshkevich[43], Marcos Dracos[5], Frédéric Druillole[20], Ran Du[1], Shuxian Du[44], Stefano Dusini[17], Martin Dvorak[42], Timo Enqvist[45], Heike Enzmann[40], Andrea Fabbri[23], Donghua Fan[46], Lei Fan[1], Jian Fang[1], Wenxing Fang[1], Marco Fargetta[7], Dmitry Fedoseev[11], Zhengyong Fei[1], Li-Cheng Feng[27], Qichun Feng[47], Richard Ford[12], Amélie Fournier[20], Haonan Gan[48], Feng Gao[8], Alberto Garfagnini[22], Arsenii Gavrikov[11], Marco Giammarchi[12], Nunzio Giudice[7], Maxim Gonchar[11], Guanghua Gong[31], Hui Gong[31], Yuri Gornushkin[11], Alexandre Göttel[49,8,78], Marco Grassi[22], Maxim Gromov[35], Vasily Gromov[11], Minghao Gu[1], Xiaofei Gu[44], Yu Gu[50], Mengyun Guan[1], Yuduo Guan[1], Nunzio Guardone[7], Cong Guo[1], Jingyuan Guo[2], Wanlei Guo[1], Xinheng Guo[51], Yuhang Guo[52], Paul Hackspacher[40], Caren Hagner[53], Ran Han[34], Yang Han[2], Miao He[1], Wei He[1], Tobias Heinz[18], Patrick Hellmuth[20], Yuekun Heng[1], Rafael Herrera[3], YuenKeung Hor[2], Shaojing Hou[1], Yee Hsiung[21], Bei-Zhen Hu[21], Hang Hu[2], Jianrun Hu[1], Jun Hu[1], Shouyang Hu[54], Tao Hu[1], Yuxiang Hu[1], Zhuojun Hu[2], Guihong Huang[46], Hanxiong Huang[54], Kaixuan Huang[2], Wenhao Huang[55,56], Xin Huang[1], Xingtao Huang[55,56], Yongbo Huang[29], Jiaqi Hui[57], Lei Huo[47], Wenju Huo[10], Cédric Huss[20], Safeer Hussain[6], Ara Ioannisian[58], Roberto Isocrate[17], Beatrice Jelmini[22], Ignacio Jeria[3], Xiaolu Ji[1], Huihui Jia[59], Junji Jia[25], Siyu Jian[54], Di Jiang[10], Wei Jiang[1], Xiaoshan Jiang[1], Xiaoping Jing[1], Cécile Jollet[20], Leonidas Kalousis[5], Philipp Kampmann[60,49], Li Kang[30], Rebin Karaparambil[19], Narine Kazarian[58], Amina Khatun[61], Khanchai Khosonthongkee[41], Denis Korablev[11], Konstantin Kouzakov[35], Alexey Krasnoperov[11], Nikolay Kutovskiy[11], Pasi Kuusiniemi[45], Tobias Lachenmaier[18], Cecilia Landini[12], Sébastien Leblanc[20], Victor Lebrin[19], Frederic Lefevre[19], Ruiting Lei[30], Rupert Leitner[42], Jason Leung[27], Daozheng Li[1], Demin Li[44], Fei Li[1], Fule Li[31], Gaosong Li[1], Huiling Li[1], Mengzhao Li[1], Min Li[1], Nan Li[1], Nan Li[62], Qingjiang Li[62], Ruhui Li[1], Rui Li[57], Shanfeng Li[30], Tao Li[2], Teng Li[55,56], Weidong Li[1,63], Weiguo Li[1], Xiaomei Li[54], Xiaonan Li[1], Xinglong Li[54], Yi Li[30], Yichen Li[1], Zepeng Li[1], Zhaohan Li[1], Zhibing Li[2], Ziyuan Li[2], Zonghai Li[25], Hao Liang[54], Hao Liang[10], Jiajun Liao[2], Ayut Limphirat[41], Guey-Lin Lin[27], Shengxin Lin[30], Tao Lin[1], Ivano Lippi[17], Fang Liu[33], Haidong Liu[44], Haotian Liu[25], Hongbang Liu[29], Hongjuan Liu[64], Hongtao Liu[2], Hui Liu[50], Jianglai Liu[57,65], Jinchang Liu[1], Min Liu[64], Qian Liu[63], Qin Liu[10], Runxuan Liu[49,8], Shubin Liu[10], Shulin Liu[1], Xiaowei Liu[2], Xiwen Liu[29], Yan Liu[1], Yunzhe Liu[1], Alexey Lokhov[35,43], Paolo Lombardi[12], Claudio Lombardo[7], Kai Loo[45], Chuan Lu[48], Jingbin Lu[66], Junguang Lu[1], Shuxiang Lu[44], Bayarto Lubsandorzhiev[43], Sultim Lubsandorzhiev[43], Livia Ludhova[49,8], Arslan Lukanov[43], Daibin Luo[1], Fengjiao Luo[64], Guang Luo[2], Shu Luo[67], Wuming Luo[1], Xiaojie Luo[1], Vladimir Lyashuk[43], Bangzheng Ma[55,56], Bing Ma[44], Qiumei Ma[1], Si Ma[1], Xiaoyan Ma[1], Xubo Ma[33], Jihane Maalmi[14], Jingyu Mai[2], Yury Malyshkin[11], Roberto Carlos Mandujano[39], Fabio Mantovani[15], Francesco Manzali[22], Xin Mao[34], Yajun Mao[68], Stefano M. Mari[23], Filippo Marini[22], Cristina Martellini[23], Gisele Martin-Chassard[14], Agnese Martini[69], Matthias Mayer[70], Davit Mayilyan[58], Ints Mednieks[71], Yue Meng[57], Anselmo Meregaglia[20], Emanuela Meroni[12], David Meyhöfer[53], Mauro Mezzetto[17], Jonathan Miller[72], Lino Miramonti[12], Paolo Montini[23], Michele Montuschi[15], Axel Müller[18], Massimiliano Nastasi[16], Dmitry V. Naumov[11], Elena Naumova[11], Diana Navas-Nicolas[14], Igor Nemchenok[11], Minh Thuan Nguyen Thi[27], Alexey Nikolaev[35], Feipeng Ning[1], Zhe Ning[1], Hiroshi Nunokawa[73], Lothar Oberauer[70], Juan Pedro Ochoa-Ricoux[3,4,39], Alexander Olshevskiy[11], Domizia Orestano[23], Fausto Ortica[37], Rainer Othegraven[40], Alessandro Paoloni[69], Sergio Parmeggiano[12], Yatian Pei[1], Nicomede Pelliccia[37], Anguo Peng[64], Haiping Peng[10], Yu Peng[1], Zhaoyuan Peng[1], Frédéric Perrot[20], Pierre-Alexandre Petitjean[38], Fabrizio Petrucci[23], Oliver Pilarczyk[40], Luis Felipe Piñeres Rico[5], Artyom Popov[35], Pascal Poussot[5], Ezio Previtali[16], Fazhi Qi[1], Ming Qi[74], Sen Qian[1], Xiaohui Qian[1], Zhen Qian[2], Hao Qiao[68], Zhonghua Qin[1], Shoukang Qiu[64], Gioacchino Ranucci[12], Neill Raper[2], Alessandra Re[12], Henning Rebber[53], Abdel Rebii[20], Mariia Redchuk[17,22], Mariia Redchuk[17,22], Bin Ren[30], Jie Ren[54], Barbara Ricci[15], Mariam Rifai[49,8], Mathieu Roche[20], Narongkiat Rodphai[13], Aldo Romani[37], Bedřich Roskovec[42], Xichao Ruan[54], Arseniy Rybnikov[11], Andrey Sadovsky[11], Paolo Saggese[12], Simone Sanfilippo[23], Anut Sangka[75], Utane Sawangwit[75],

Julia Sawatzki[70], Michaela Schever[49,8], Cédric Schwab[5], Konstantin Schweizer[70], Alexandr Selyunin[11], Andrea Serafini[22], Giulio Settanta[49,77], Mariangela Settimo[19], Zhuang Shao[52], Vladislav Sharov[11], Arina Shaydurova[11], Jingyan Shi[1], Yanan Shi[1], Vitaly Shutov[11], Andrey Sidorenkov[43], Fedor Šimkovic[61], Chiara Sirignano[22], Jaruchit Siripak[41], Monica Sisti[16], Maciej Slupecki[45], Mikhail Smirnov[2], Oleg Smirnov[11], Thiago Sogo-Bezerra[19], Sergey Sokolov[11], Julanan Songwadhana[41], Boonrucksar Soonthornthum[75], Albert Sotnikov[11], Ondřej Šrámek[42], Warintorn Sreethawong[41], Achim Stahl[8], Luca Stanco[17], Konstantin Stankevich[35], Dušan Štefánik[61], Hans Steiger[40,70], Jochen Steinmann[8], Tobias Sterr[18], Matthias Raphael Stock[70], Virginia Strati[15], Alexander Studenikin[35], Jun Su[2], Shifeng Sun[33], Xilei Sun[1], Yongjie Sun[10], Yongzhao Sun[1], Zhengyang Sun[57], Narumon Suwonjandee[13], Michal Szelezniak[5], Jian Tang[2], Qiang Tang[2], Quan Tang[64], Xiao Tang[1], Alexander Tietzsch[18], Igor Tkachev[43], Tomas Tmej[42], Marco Danilo Claudio Torri[12], Konstantin Treskov[11], Andrea Triossi[22], Giancarlo Troni[3], Wladyslaw Trzaska[45], Cristina Tuve[7], Nikita Ushakov[43], Vadim Vedin[71], Giuseppe Verde[7], Maxim Vialkov[35], Benoit Viaud[19], Cornelius Moritz Vollbrecht[49,8], Cristina Volpe[14], Katharina von Sturm[22], Vit Vorobel[42], Dmitriy Voronin[43], Lucia Votano[69], Pablo Walker[3,4], Caishen Wang[30], Chung-Hsiang Wang[28], En Wang[44], Guoli Wang[47], Jian Wang[10], Jun Wang[2], Lu Wang[1], Meifen Wang[1], Meng Wang[64], Meng Wang[55,56], Ruiguang Wang[1], Siguang Wang[68], Wei Wang[74], Wei Wang[2], Wenshuai Wang[1], Xi Wang[62], Xiangyue Wang[2], Yangfu Wang[1], Yaoguang Wang[1], Yi Wang[31], Yi Wang[46], Yifang Wang[1], Yuanqing Wang[31], Yuman Wang[74], Zhe Wang[31], Zheng Wang[1], Zhimin Wang[1], Zongyi Wang[31], Apimook Watcharangkool[75], Wei Wei[1], Wei Wei[55,56], Wenlu Wei[1], Yadong Wei[30], Kaile Wen[1], Liangjian Wen[1], Christopher Wiebusch[8], Steven Chan-Fai Wong[2], Bjoern Wonsak[53], Diru Wu[1], Qun Wu[55,56], Zhi Wu[1], Michael Wurm[40], Jacques Wurtz[5], Christian Wysotzki[8], Yufei Xi[48], Dongmei Xia[76], Xiang Xiao[2], Xiaochuan Xie[29], Yuguang Xie[1], Zhangquan Xie[1], Zhao Xin[1], Zhizhong Xing[1], Benda Xu[31], Cheng Xu[64], Donglian Xu[57,65], Fanrong Xu[50], Hangkun Xu[1], Jilei Xu[1], Jing Xu[51], Meihang Xu[1], Yin Xu[59], Yu Xu[2], Baojun Yan[1], Taylor Yan[41], Wenqi Yan[1], Xiongbo Yan[1], Yupeng Yan[41], Changgen Yang[1], Chengfeng Yang[29], Huan Yang[1], Jie Yang[44], Lei Yang[30], Xiaoyu Yang[1], Yifan Yang[1], Yifan Yang[38], Haifeng Yao[1], Jiaxuan Ye[1], Mei Ye[1], Ziping Ye[65], Frédéric Yermia[19], Na Yin[55,56], Zhengyun You[2], Boxiang Yu[1], Chiye Yu[30], Chunxu Yu[59], Hongzhao Yu[2], Miao Yu[25], Xianghui Yu[59], Zezhong Yu[1], Cenxi Yuan[2], Chengzhuo Yuan[1], Ying Yuan[68], Zhenxiong Yuan[31], Noman Zafar[6], Vitalii Zavadskyi[11], Shan Zeng[1], Tingxuan Zeng[1], Yuda Zeng[2], Liang Zhan[1], Aiqiang Zhang[31], Bin Zhang[44], Binting Zhang[1], Feiyang Zhang[57], Guoqing Zhang[1], Honghao Zhang[2], Jialiang Zhang[74], Jiawen Zhang[1], Jie Zhang[1], Jin Zhang[29], Jingbo Zhang[47], Jinnan Zhang[1], Mohan Zhang[1], Peng Zhang[1], Qingmin Zhang[52], Shiqi Zhang[2], Shu Zhang[2], Tao Zhang[57], Xiaomei Zhang[1], Xin Zhang[1], Xuantong Zhang[1], Xueyao Zhang[55,56], Yinhong Zhang[1], Yiyu Zhang[1], Yongpeng Zhang[1], Yu Zhang[1], Yuanyuan Zhang[57], Yumei Zhang[2], Zhenyu Zhang[25], Zhijian Zhang[30], Fengyi Zhao[32], Rong Zhao[2], Runze Zhao[1], Shujun Zhao[44], Dongqin Zheng[50], Hua Zheng[30], Yangheng Zheng[63], Weirong Zhong[50], Jing Zhou[54], Li Zhou[1], Nan Zhou[10], Shun Zhou[1], Tong Zhou[1], Xiang Zhou[25], Jiang Zhu[2], Jingsen Zhu[9], Kangfu Zhu[52], Kejun Zhu[1], Zhihang Zhu[1], Bo Zhuang[1], Honglin Zhuang[1], Liang Zong[31], and Jiaheng Zou[1]

[1] Institute of High Energy Physics, Beijing, People's Republic of China; liyufeng@ihep.ac.cn
[2] Sun Yat-Sen University, Guangzhou, People's Republic of China; lingjj5@mail.sysu.edu.cn
[3] Pontificia Universidad Católica de Chile, Santiago, Chile
[4] Millennium Institute for SubAtomic Physics at the High-energy Frontier (SAPHIR), ANID, Chile
[5] IPHC, Université de Strasbourg, CNRS/IN2P3, F-67037 Strasbourg, France
[6] Pakistan Institute of Nuclear Science and Technology, Islamabad, Pakistan
[7] INFN Catania and Dipartimento di Fisica e Astronomia dell Università di Catania, Catania, Italy
[8] III. Physikalisches Institut B, RWTH Aachen University, Aachen, Germany
[9] East China University of Science and Technology, Shanghai, People's Republic of China
[10] University of Science and Technology of China, Hefei, People's Republic of China
[11] Joint Institute for Nuclear Research, Dubna, Russia
[12] INFN Sezione di Milano and Dipartimento di Fisica dell Università di Milano, Milano, Italy
[13] Department of Physics, Faculty of Science, Chulalongkorn University, Bangkok, Thailand
[14] IJCLab, Université Paris-Saclay, CNRS/IN2P3, 91405 Orsay, France
[15] Department of Physics and Earth Science, University of Ferrara and INFN Sezione di Ferrara, Ferrara, Italy
[16] INFN Milano Bicocca and University of Milano Bicocca, Milano, Italy
[17] INFN Sezione di Padova, Padova, Italy
[18] Eberhard Karls Universität Tübingen, Physikalisches Institut, Tübingen, Germany
[19] SUBATECH, Nantes Université, IMT Atlantique, CNRS-IN2P3, Nantes, France
[20] Université Bordeaux, CNRS, LP2i Bordeaux, UMR 5797, F-33170 Gradignan, France
[21] Department of Physics, National Taiwan University, Taipei
[22] Dipartimento di Fisica e Astronomia dell'Università di Padova and INFN Sezione di Padova, Padova, Italy
[23] University of Roma Tre and INFN Sezione Roma Tre, Roma, Italy
[24] Centre de Physique des Particules de Marseille, Marseille, France
[25] Wuhan University, Wuhan, People's Republic of China
[26] INFN Milano Bicocca and Politecnico of Milano, Milano, Italy
[27] Institute of Physics, National Yang Ming Chiao Tung University, Hsinchu
[28] National United University, Miao-Li
[29] Guangxi University, Nanning, People's Republic of China
[30] Dongguan University of Technology, Dongguan, People's Republic of China
[31] Tsinghua University, Beijing, People's Republic of China
[32] Institute of Modern Physics, Chinese Academy of Sciences, Lanzhou, People's Republic of China
[33] North China Electric Power University, Beijing, People's Republic of China
[34] Beijing Institute of Spacecraft Environment Engineering, Beijing, People's Republic of China
[35] Lomonosov Moscow State University, Moscow, Russia
[36] Universidade Estadual de Londrina, Londrina, Brazil
[37] INFN Sezione di Perugia and Dipartimento di Chimica, Biologia e Biotecnologie dell'Università di Perugia, Perugia, Italy

[38] Université Libre de Bruxelles, Brussels, Belgium
[39] Department of Physics and Astronomy, University of California, Irvine, CA, USA
[40] Institute of Physics and EC PRISMA$^+$, Johannes Gutenberg Universität Mainz, Mainz, Germany
[41] Suranaree University of Technology, Nakhon Ratchasima, Thailand
[42] Charles University, Faculty of Mathematics and Physics, Prague, Czech Republic
[43] Institute for Nuclear Research of the Russian Academy of Sciences, Moscow, Russia
[44] School of Physics and Microelectronics, Zhengzhou University, Zhengzhou, People's Republic of China
[45] University of Jyvaskyla, Department of Physics, Jyvaskyla, Finland
[46] Wuyi University, Jiangmen, People's Republic of China
[47] Harbin Institute of Technology, Harbin, People's Republic of China
[48] Institute of Hydrogeology and Environmental Geology, Chinese Academy of Geological Sciences, Shijiazhuang, People's Republic of China
[49] Forschungszentrum Jülich GmbH, Nuclear Physics Institute IKP-2, Jülich, Germany
[50] Jinan University, Guangzhou, People's Republic of China
[51] Beijing Normal University, Beijing, People's Republic of China
[52] Xi'an Jiaotong University, Xi'an, People's Republic of China
[53] Institute of Experimental Physics, University of Hamburg, Hamburg, Germany
[54] China Institute of Atomic Energy, Beijing, People's Republic of China
[55] Shandong University, Jinan, People's Republic of China
[56] Key Laboratory of Particle Physics and Particle Irradiation of Ministry of Education, Shandong University, Qingdao, People's Republic of China
[57] School of Physics and Astronomy, Shanghai Jiao Tong University, Shanghai, People's Republic of China
[58] Yerevan Physics Institute, Yerevan, Armenia
[59] Nankai University, Tianjin, People's Republic of China
[60] Helmholtzzentrum für Schwerionenforschung, Planckstrasse 1, D-64291 Darmstadt, Germany
[61] Comenius University Bratislava, Faculty of Mathematics, Physics and Informatics, Bratislava, Slovakia
[62] College of Electronic Science and Engineering, National University of Defense Technology, Changsha, People's Republic of China
[63] University of Chinese Academy of Sciences, Beijing, People's Republic of China
[64] The Radiochemistry and Nuclear Chemistry Group in University of South China, Hengyang, People's Republic of China
[65] Tsung-Dao Lee Institute, Shanghai Jiao Tong University, Shanghai, People's Republic of China
[66] Jilin University, Changchun, People's Republic of China
[67] Xiamen University, Xiamen, People's Republic of China
[68] School of Physics, Peking University, Beijing, People's Republic of China
[69] Laboratori Nazionali di Frascati dell'INFN, Roma, Italy
[70] Technische Universität München, München, Germany
[71] Institute of Electronics and Computer Science, Riga, Latvia
[72] Universidad Tecnica Federico Santa Maria, Valparaiso, Chile
[73] Pontificia Universidade Catolica do Rio de Janeiro, Rio de Janeiro, Brazil
[74] Nanjing University, Nanjing, People's Republic of China
[75] National Astronomical Research Institute of Thailand, Chiang Mai, Thailand
[76] Chongqing University, Chongqing, People's Republic of China
Received 2022 October 17; revised 2024 February 7; accepted 2024 February 12; published 2024 April 12

Abstract

The physics potential of detecting ^{8}B solar neutrinos will be exploited at the Jiangmen Underground Neutrino Observatory (JUNO), in a model-independent manner by using three distinct channels of the charged current (CC), neutral current (NC), and elastic scattering (ES) interactions. Due to the largest-ever mass of ^{13}C nuclei in the liquid scintillator detectors and the expected low background level, ^{8}B solar neutrinos are observable in the CC and NC interactions on ^{13}C for the first time. By virtue of optimized event selections and muon veto strategies, backgrounds from the accidental coincidence, muon-induced isotopes, and external backgrounds can be greatly suppressed. Excellent signal-to-background ratios can be achieved in the CC, NC, and ES channels to guarantee the observation of the ^{8}B solar neutrinos. From the sensitivity studies performed in this work, we show that JUNO, with 10 yr of data, can reach the 1σ precision levels of 5%, 8%, and 20% for the ^{8}B neutrino flux, $\sin^2\theta_{12}$, and Δm^2_{21}, respectively. Probing the details of both solar physics and neutrino physics would be unique and helpful. In addition, when combined with the Sudbury Neutrino Observatory measurement, the world's best precision of 3% is expected for the measurement of the ^{8}B neutrino flux.

Unified Astronomy Thesaurus concepts: Solar neutrinos (1511)

1. Introduction

Electron neutrino fluxes are produced from thermal nuclear fusion reactions in the solar core, either through the proton–proton (pp) chain or the carbon–nitrogen–oxygen (CNO) cycle. According to their production reactions, the solar neutrino species can be categorized as pp, ^{7}Be, pep, ^{8}B, *hep* neutrinos of the pp chain, and the ^{13}N, ^{15}O, and ^{17}F neutrinos of the CNO cycle. Before reaching the detector, solar neutrinos undergo flavor conversion inside the Sun and Earth during their propagation. Solar neutrino measurements have a long history starting with the measurements done by the Homestake experiment (Davis et al. 1968). Many measurements, such as those of Homestake (Davis et al. 1968), Kamiokande (Hirata et al. 1989), GALLEX/GNO (Anselmann et al. 1993; Altmann et al. 2000), SAGE (Abazov et al. 1991), and SuperKamiokande (SK; Fukuda et al. 1998, 2001), observed the solar

[77] Now at Istituto Superiore per la Protezione e la Ricerca Ambientale, Via Vitaliano Brancati, 48, 00144 Roma, Italy.
[78] Now at Gravity Exploration Institute, Cardiff University, Cardiff CF24 3AA, UK.

Original content from this work may be used under the terms of the Creative Commons Attribution 4.0 licence. Any further distribution of this work must maintain attribution to the author(s) and the title of the work, journal citation and DOI.

neutrino deficit problem: that is, the number of observed neutrinos originating from the Sun was much less than that expected from the standard solar model (SSM). Subsequently, the Sudbury Neutrino Observatory (SNO) provided the first model-independent evidence of solar neutrino flavor conversion using three distinct neutrino interaction channels in heavy water (Chen 1985; Ahmad et al. 2001, 2002; Ahmed et al. 2004; Aharmim et al. 2008, 2013a, 2013b). These reactions are the ν_e sensitive charged current (CC) interaction, all flavor sensitive neutral current (NC) interaction on deuterium, and the elastic scattering (ES) interaction on electrons from all neutrino flavors with different cross sections.

Solar neutrino observations rely on the SSM flux predictions, the neutrino oscillation parameters, and the solar density model, which determine the flavor conversion (Wolfenstein 1978; Mikheev & Smirnov 1985; Zyla et al. 2020). Thus, although SK (Renshaw et al. 2014; Abe et al. 2016) and Borexino (Bellini et al. 2014; Agostini et al. 2020) experiments have made precision measurements on the ^{8}B neutrinos via the ES interaction, the evaluation of the total amount of neutrinos produced inside the Sun relies on the input of solar neutrino oscillations (Zyla et al. 2020). The present most precise ^{8}B neutrino flux is determined by SNO with a 1σ confidence level uncertainly of around 3.8% (Ahmad et al. 2002; Ahmed et al. 2004; Aharmim et al. 2008, 2013a, 2013b), and it is the only existing model-independent flux measurement. Therefore, a second independent measurement of the total ^{8}B neutrino flux with the NC channel (Arafune et al. 1989; Ianni et al. 2005) would be important in answering relevant questions in the field of solar physics. For example, there is the solar abundance problem, in which the SSM based on the solar composition with a higher value of metallicity is inconsistent with the helioseismological measurements (Vinyoles et al. 2017). Note that a recent solar model is able to resolve the discord between the helioseismological and photospheric measurements (Magg et al. 2022), but lively discussions on this topic are still ongoing (Yang 2022; Buldgen et al. 2023).

In contrast, the neutrino oscillation parameters $\sin^2\theta_{12}$ and Δm^2_{21} have reached the 1σ confidence level uncertainty of around 5% and 15%, respectively, from the current global solar neutrino data (Esteban et al. 2020). The mixing angle $\sin^2\theta_{12}$ is extracted from the comparison of the observed fluxes of pp, ^{7}Be, and ^{8}B solar neutrinos to their respective total fluxes from the SSM. And the mass squared difference Δm^2_{21} is measured from both the vacuum–matter transition of the ^{8}B neutrino oscillations and the size of the day–night asymmetry. A direct comparison of oscillation parameters from the solar neutrino and reactor antineutrino oscillations is a unique probe of new physics beyond the Standard Model of particle physics. It would be excellent to have a new measurement of solar neutrino oscillations with high precision in this respect. This has triggered a variety of interesting discussions on the prospects of future large neutrino detectors (Beacom et al. 2017; Abe et al. 2018; Capozzi et al. 2019; Abusleme et al. 2021a).

The Jianmen Underground Neutrino Observatory (JUNO) is a 20 kt liquid scintillator (LS) detector located in South China and will start acquiring data by 2024. As a multiple-purpose neutrino experiment, JUNO is unique for solar neutrino detection because of its large target mass, excellent energy resolution, and expected low background levels. With the analysis threshold cut of around 2 MeV for the recoiled electron energies in the ES channel, JUNO can make a high statistics measurement of the flux and spectral shape of ^{8}B solar neutrinos and will be able to extract the neutrino oscillation parameters $\sin^2\theta_{12}$ and Δm^2_{21} (Abusleme et al. 2021a). In addition to the high statistics measurement in the ES channel, the presence of the large mass of the ^{13}C nuclei ($\sim$0.2 kt) makes it feasible to detect ^{8}B solar neutrinos via CC and NC interactions on ^{13}C. By combining the CC, NC, and ES channels, we are able to perform a model-independent measurement of the ^{8}B solar neutrino flux and oscillation parameters $\sin^2\theta_{12}$ and Δm^2_{21}, which will add a unique contribution to the global solar neutrino program.

This paper is organized as follows. We illustrate the typical signatures of the CC and NC interactions of ^{8}B solar neutrinos and evaluate the corresponding backgrounds in the JUNO detector in Section 2. In Section 3, the physics potential of detecting ^{8}B solar neutrinos with different combinations of CC, NC, and ES channels is presented, and the sensitivity to the ^{8}B solar neutrino flux, $\sin^2\theta_{12}$ and Δm^2_{21} is reported. The concluding remarks of this study are presented in Section 4.

2. Signal and Background at JUNO

The JUNO experiment is building the world's largest LS detector with a total target mass of 20 kt, in which the mass fraction of carbon is 88%. Given that the natural abundance of ^{13}C is 1.1%, the total mass of ^{13}C reaches 193.6 tons, which is similar to the total deuterium mass of 200 tons for the SNO detector. Considering the preferable cross sections of ^{13}C at solar neutrino energies (Fukugita et al. 1988; Suzuki et al. 2012, 2019), the CC and NC solar neutrino rates on ^{13}C will be rather sizable in the JUNO detector.

In Table 1, we present the typical CC, NC, and ES detection channels for ^{8}B solar neutrinos in the LS medium. For each interaction channel, the reaction threshold is provided, together with the typical experimental signatures, and the expected event numbers for 10 yr of data taking before event selection cuts. The spin and parity of the daughter nuclei at the ground (gnd) or excited state, denoted by the corresponding excited energies, are also provided. The unoscillated ^{8}B solar neutrino ν_e flux ($5.25\times10^6/\mathrm{cm}^2\,\mathrm{s}^{-1}$) is taken from the final result from SNO for this estimation (Aharmim et al. 2013b), and the spectrum is taken from Bahcall et al. (1996) and Bahcall (1997). The cross sections for these exclusive channels are taken from the calculation in Fukugita et al. (1988) and Suzuki et al. (2012, 2019), in which the uncertainties at the level of a few percent are considered to be achievable. Note that the standard Mikheev–Smirnov–Wolfenstein (MSW) effect of solar neutrino oscillations (Wolfenstein 1978; Mikheev & Smirnov 1985) and the neutrino oscillation parameters from Zyla et al. (2020) are used in the calculation of the signals of the CC, NC, and ES channels.

There are no interactions on the ^{12}C nuclei for most solar neutrinos because of the high energy threshold. Thus, for the CC channel, we are left with the following two exclusive interactions:

$$\nu_e + {}^{13}\mathrm{C} \rightarrow e^- + {}^{13}\mathrm{N}\left(\frac{1}{2}^-;\ \mathrm{gnd}\right), \tag{1}$$

$$\nu_e + {}^{13}\mathrm{C} \rightarrow e^- + {}^{13}\mathrm{N}\left(\frac{3}{2}^-;\ 3.502\ \mathrm{MeV}\right), \tag{2}$$

where the final ^{13}N is in the ground state and excited ^{13}N($3/2^-$; 3.502 MeV) state, respectively. For the first reaction channel, the ground state of ^{13}N undergoes a delayed β^+ decay

Table 1
Typical CC, NC, and ES Detection Channels of the ^{8}B Solar Neutrinos Together with the Final States, Neutrino Energy Threshold, Typical Signatures in the Detector, and Expected Event Numbers with 10 yr of Data Taking

No.		Channels	Threshold (MeV)	Signal	Event Numbers (10 yr)
1		$\nu_e + {}^{12}\mathrm{C} \rightarrow e^- + {}^{12}\mathrm{N}(1^+;\ \mathrm{gnd})$ (Fukugita et al. 1988)	16.827	$e^- + {}^{12}\mathrm{N}$ decay (β^+, $Q = 17.338$ MeV)	0.43
1	CC	$\nu_e + {}^{13}\mathrm{C} \rightarrow e^- + {}^{13}\mathrm{N}(\frac{1}{2}^-;\ \mathrm{gnd})$ (Suzuki et al. 2012)	2.2	$e^- + {}^{13}\mathrm{N}$ decay (β^+, $Q = 2.22$ MeV)	3929
2		$\nu_e + {}^{13}\mathrm{C} \rightarrow e^- + {}^{13}\mathrm{N}(\frac{3}{2}^-;\ 3.5\ \mathrm{MeV})$ (Suzuki et al. 2012)	5.7	$e^- + p$	2464
4		$\nu_x + {}^{12}\mathrm{C} \rightarrow \nu_x + {}^{12}\mathrm{C}(1^+;\ 15.11\ \mathrm{MeV})$ (Fukugita et al. 1988)	15.1	γ	4.8
3	NC	$\nu_x + {}^{13}\mathrm{C} \rightarrow \nu_x + n + {}^{12}\mathrm{C}(2^+;\ 4.44\ \mathrm{MeV})$ (Suzuki et al. 2019)	6.864	$\gamma + n$ capture	65
4		$\nu_x + {}^{13}\mathrm{C} \rightarrow \nu_x + {}^{13}\mathrm{C}(\frac{1}{2}^+;\ 3.089\ \mathrm{MeV})$ (Suzuki et al. 2012)	3.089	γ	14
5		$\nu_x + {}^{13}\mathrm{C} \rightarrow \nu_x + {}^{13}\mathrm{C}(\frac{3}{2}^-;\ 3.685\ \mathrm{MeV})$ (Suzuki et al. 2012)	3.685	γ	3032
6		$\nu_x + {}^{13}\mathrm{C} \rightarrow \nu_x + {}^{13}\mathrm{C}(\frac{5}{2}^+;\ 3.854\ \mathrm{MeV})$ (Suzuki et al. 2012)	3.854	γ	2.8
7	ES	$\nu_x + e \rightarrow \nu_x + e$	0	e^-	3.0×10^5

Note. Note that ν_x with ($x = e, \mu, \tau$) denotes all three active flavor neutrinos. The spin and parity of the daughter nuclei at the gnd or excited states, denoted as the corresponding excited energies, are also provided.

($Q = 2.2$ MeV) with a lifetime of 863 s. The distinct signature for this channel is a coincidence of the prompt electron and delayed positron with stringent time, distance, and energy requirements. The expected number of events for ^{8}B solar neutrinos in this coincidence channel is 3929 with 10 yr of data taking. On the other hand, although the channel with an excited $^{13}\mathrm{N}(3/2^-;\ 3.502\ \mathrm{MeV})$ has a comparable cross section as the ground-state channel (Suzuki et al. 2012), the corresponding signature after quenching is a single event since the deexcitation of $^{13}\mathrm{N}(3/2^-;\ 3.502\ \mathrm{MeV})$ is dominated by a proton knockout, and thus, cannot be distinguished from the recoiled electron of the ES channel and the single γ of the NC channel on an event-by-event basis. Therefore, in the coincidence event category, we focus on the CC channel with the ground-state ^{13}N and consider the channel with the excited $^{13}\mathrm{N}(3/2^-;\ 3.502\ \mathrm{MeV})$ as a component of the total spectrum of the singles as illustrated in Figure 2.

Among the five listed NC channels, the only one with a coincidence signature is the interaction of $\nu_x + {}^{13}\mathrm{C} \rightarrow \nu_x + n + {}^{12}\mathrm{C}$, with a prompt γ energy of 4.44 MeV from ^{12}C deexcitation and the delayed neutron capture. However, given that the background from the inverse beta decay (IBD) interactions of reactor antineutrinos are overwhelming, where the signal-to-background ratio is at the level of 10^{-4}, the event rate of this channel is unobservable. In this work, we focus on the NC channels with the signature of single γ deexcitation, among which the NC interaction with the ^{13}C deexcited energy of 3.685 MeV:

$$\nu_x + {}^{13}\mathrm{C} \rightarrow \nu_x + {}^{13}\mathrm{C}\left(\frac{3}{2}^-;\ 3.685\ \mathrm{MeV}\right) \tag{3}$$

is the dominant interaction channel and will be used to determine the ^{8}B solar neutrino flux via the NC interaction.

Finally, we also consider the ES interaction channel on the electron,

$$\nu_x + e \rightarrow \nu_x + e, \tag{4}$$

where the signature is a single recoiled electron (Abusleme et al. 2021a). Using all three channels of the CC, NC, and ES interactions, we are able to make a model-independent measurement of the ^{8}B solar neutrino flux, $\sin^2\theta_{12}$ and Δm^2_{21} with JUNO, which is useful in disentangling the solar dynamics and the neutrino oscillation effects. This measurement is expected to be the only model-independent study after the SNO experiment (Ahmad et al. 2001, 2002; Ahmed et al. 2004; Aharmim et al. 2008).

To summarize, in this work, we are going to employ the following three interaction channels for a model-independent approach of the JUNO ^{8}B solar neutrino program: (i) the CC detection channel is sensitive to the ν_e component of solar neutrinos, (ii) the NC channel is sensitive to all active neutrino flavors (ν_e, ν_μ, ν_τ) with identical cross sections, and (iii) the ES channel is also sensitive to all active flavors, but with a preferred cross section for the ν_e flux (i.e., $\sigma(\nu_{\mu/\tau}) \simeq 0.17\,\sigma(\nu_e)$).

2.1. $\nu_e + {}^{13}$C CC Channel

For the typical coincidence signature of the CC channel, $\nu_e + {}^{13}\mathrm{C} \rightarrow e^- + {}^{13}\mathrm{N}(1/2^-;\ \mathrm{gnd})$, the energy of the prompt signal is the kinetic energy of the outgoing electron with the reaction threshold of 2.2 MeV. Therefore, there is a one-to-one correspondence between the electron kinetic energy and the initial neutrino energy $T_e \simeq E_\nu - 2.2$ MeV because of the negligible recoil energy of the daughter ^{13}N. Meanwhile, the delayed signal is the deposited energy of the positron from the ^{13}N β^+ decay ($Q = 2.2$ MeV), with a decay lifetime of $\tau = 863$ s. The time and spatial correlation between the prompt and delayed signals provides the distinct feature of the coincidence signature.

In the following, we consider two significant backgrounds for this coincidence signature of the CC channel in this work.

1. The first background is the accidental coincidence of two single events. For the visible energy between 2 and 5 MeV, natural radioactivity composes the most significant part of the prompt component of the coincidence candidate, while the prompt background events above 5 MeV come from the muon-induced unstable isotopes and the recoiled electrons of solar neutrino ES interactions. Due to the expected natural radioactivity level in the LS (10^{-17} g/g ^{238}U and ^{232}Th in the secular equilibrium, 10^{-18} g/g ^{40}K and 10^{-24} g/g ^{210}Pb), a requirement on the selection of the prompt energy is to minimize the contribution from these radioactivity events.

Table 2
Efficiencies of Optimized Event Selection Cuts for the Signal and Backgrounds of the ν_e CC Channel [$\nu_e + {}^{13}\mathrm{C} \rightarrow e^- + {}^{13}\mathrm{N}(1/2^-;\ \mathrm{gnd})$] Analysis

	Cuts	CC Signal Efficiency	CC Signal	Background for CC Channel		
				Solar ES Accidental	Muon-induced Isotopes	
					Accidental	Correlated
…	…	…	3929	…	…	…
Time cut	4 ms $< \Delta T <$ 900 s	65%	2554	10^{10}	10^{13}	10^{12}
Energy cut	5 MeV $< E_p <$ 14 MeV 1 MeV $< E_d <$ 2 MeV	79% 91%	1836	10^9	10^{10}	10^9
Fiducial volume cut	$R <$ 16.5 m (Abusleme et al. 2021a)	81%	1487	10^7	10^7	10^8
Vertex cut	$\Delta d <$ 0.47 m	87%	1293	328	10^5	10^6
Muon veto	Muon and TFC veto (Abusleme et al. 2021a)	50%	647	164	53	58
Combined	…	17%	647		275	

Note. The expected event numbers of the signal and backgrounds for 10 yr of data taking after each cut are also listed. The fiducial volume used in this work corresponds to the effective mass of 16.2 kt. For the energy cuts, E_p and E_d represent the visible energy of prompt and delayed signals. The same muon and threefold-coincidence veto strategies as in Abusleme et al. (2021a) are used for the reduction of muon-induced isotopes.

The delayed component of the accidental background is mainly from the cosmogenic ^{11}C decay ($Q = 1.98$ MeV) in the energy range of [1, 2] MeV, while the internal LS radioactivity contributes less than 2% compared to that from ^{11}C. If the internal radioactivity is 1–2 orders of magnitude higher than expected, the contribution to the delayed component from the radioactivity would be at the same level as the cosmogenic ^{11}C decay. Note that all the single events in the energy range between 1 and 2 MeV can be accurately measured in situ with future data, and the accidental background can be deduced with the off-time coincidence method. Note that we have neglected the external radioactivity, which can be effectively removed by the proper fiducial volume cut.

2. The second background is produced by the correlated prompt and delayed decays of unstable isotopes from the same parent muon. These correlated decays are not considered in the above accidental background. Therefore, the cosmic muon and the corresponding isotope simulations have been performed, and the muon veto strategies of the threefold coincidence are the same as those in Abusleme et al. (2021a). This shows that the prompt signal is mainly from the beta decays of ^{12}B, ^{8}Li, ^{6}He, and ^{10}C (below 4 MeV), and as expected the delayed signal is from ^{11}C. The muon detection efficiency of the outer water veto can reach as high as 99.5% (Abusleme et al. 2021a). Since the remaining untagged muons are usually located at the edge of the central detector, this muon-induced correlated background can be removed using the fiducial volume cut and is neglected in this work. Note that we have assumed a perfect detector uniformity for these isotopes and used the whole detector region to estimate the background inside the fiducial volume.

We have simulated the signal and backgrounds using the official JUNO simulation software (Zou et al. 2015; Lin et al. 2017). According to the signal characteristics of the CC channel, the accidental background can be calculated with different selection cuts. The final event selection criteria are obtained by optimizing the figure of merit, $S/\sqrt{S+B}$, where S and B stand for the rates of the signal and background, respectively. The optimized event selection cuts of the fiducial volume, prompt and delayed energies, time and spatial correlation cuts, and muon vetos are provided step by step in Table 2, where the efficiencies of the signal and backgrounds are also calculated. In order to avoid possible large contamination from the internal radioactivity and muon-induced ^{10}C, we select the threshold of the prompt visible energy to 5 MeV for the CC channel, i.e., 5 MeV $< E_p <$ 14 MeV. Meanwhile, the fiducial volume is chosen to be $R < 16.5$ m to reject the external radioactivity and isotopes, with R being the distance to the detector center. It should be noted that an anticoincidence criterion with a time distance cut of $\Delta T > 4$ ms has been used to reject the IBD interactions of reactor antineutrinos, achieving a rejection power of 100%. Meanwhile, this IBD rejection cut has a negligible impact on the signal because of the much longer lifetime of ^{13}N.

We illustrate in Figure 1 the expected prompt visible energy spectra of the selected signal and residual backgrounds in the CC channel after the optimized cuts. The expected number of selected signals is 647 for 10 yr of data taking is shown as the purple line. The fiducial volume used in this work corresponds to the effective mass of 16.2 kt. The accidental background with solar neutrino ES interactions as the prompt signal is illustrated as the green line and contributes 164 background events, which will be fully correlated with the solar neutrino ES signal in the following global analysis. In contrast, the muon-induced isotopes contribute 111 background events (depicted as the red line of Figure 1), which are from both the accidental coincidence (53 events) and correlated background (58 events). Therefore, we can achieve an excellent $S/\sqrt{S+B} \simeq 21$, offering an excellent prospect for future experimental measurements. As a comparison, a preliminary study assessing the feasibility of detecting solar neutrinos via the CC interactions on ^{13}C in the Borexino experiment has been previously reported in the thesis of Ghiano (2012), where an upper limit for the number of the solar neutrino CC interaction ^{13}C was established, constrained by the limited event statistics.

Finally, the expected event number of *hep* solar neutrinos in the CC channel is about 15 for 10 yr of data taking, but only three events are beyond the spectral tail of ^{8}B solar neutrinos.

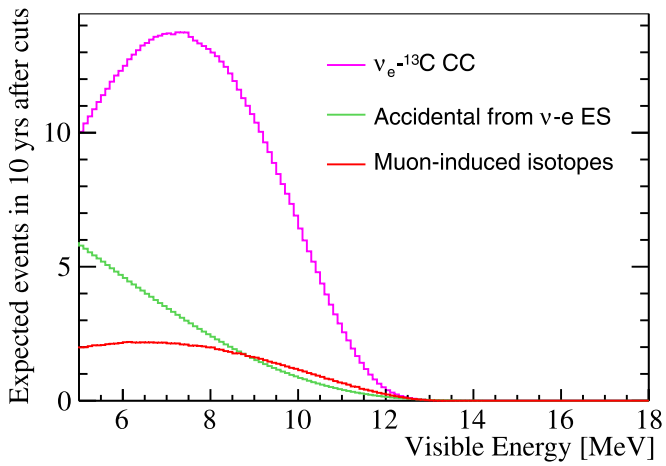

Figure 1. Expected prompt visible energy spectra of the CC signal and backgrounds after the optimized cuts. The *y*-axis represents the number of events per 0.1 MeV. The accidental background with the recoiled electron from solar neutrino ES interaction as the prompt signal is illustrated as the green line. The background from muon-induced isotopes is illustrated as the red line, which is the summation of the accidental and correlated backgrounds originating from the initial muons.

Thus, it would be difficult to detect the *hep* solar neutrinos with the CC interaction on ^{13}C, and the signal from the *hep* solar neutrinos will be neglected in this work.

2.2. ν_x+^{13}C NC Channel

The typical signature for the NC event, ν_x+^{13}C $\rightarrow \nu_x$+ ^{13}C(3/2$^-$; 3.685 MeV) is a monoenergetic γ with an energy of 3.685 MeV, convoluted with the energy resolution of $\sigma_E/E = 3\%/\sqrt{E\ (\mathrm{MeV})}$ for the JUNO detector. The expected visible energy spectra of all single event sources for 10 yr of data taking with the same energy-dependent fiducial volume cuts as in Abusleme et al. (2021a) are shown in Figure 2. The blue and green curves represent singles from the ν_x+^{13}C NC and $\nu_x + e$ ES channels, respectively. The purple curve includes the ν_e+^{13}C $\rightarrow e^-$+^{13}N(3/2$^-$; 3.502 MeV) channel and the residual singles of the ν_e+^{13}C $\rightarrow e^-$+^{13}N(1/2$^-$; gnd) channel after the coincidence cut. The anticoincidence criterion successfully reduces residual singles from reactor antineutrino IBD interactions to a negligible level. These residuals are due to cases where prompt and delayed signals appear in the same 1 μs readout window. The red curve represents the single events from natural radioactivity and muon-induced unstable isotopes (Abusleme et al. 2021a). The brown curve includes the $\bar{\nu}_e + e$ ES and $\bar{\nu}_x$ +^{13} C NC channels from reactor antineutrinos. The NC events rate from reactor antineutrinos is less than 0.2% of that from solar neutrinos. The black curve is the summation of all the components. Note that the discontinuities at 3 and 5 MeV are caused by the energy-dependent fiducial volume cuts which are, from low to high energies, $R < 13$ m for [2, 3] MeV, $R < 15$ m for [3, 5] MeV, and $R < 16.5$ m for the energies larger than 5 MeV. The upper right insert plot is illustrated for the energy range between 3 and 5 MeV in the linear scale, where a clear peak from the solar neutrino NC channel can be seen above the continuous spectra from solar neutrino ES interactions and the other backgrounds, demonstrating the promising prospect for the observation of the NC channel at JUNO. After all the cuts the number of signal events in the NC channel is 738 for 10 yr of data taking.

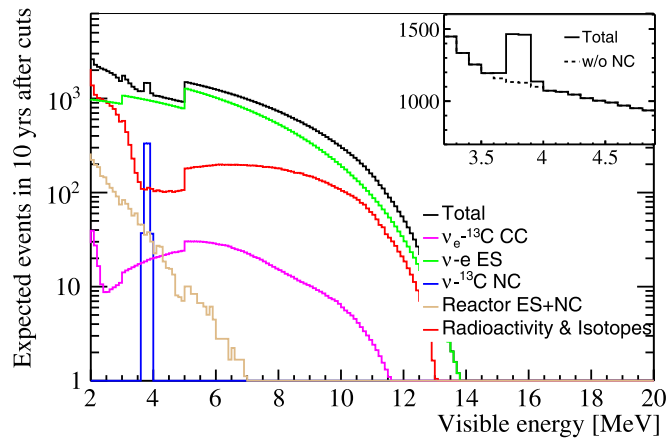

Figure 2. Expected visible energy spectra of all single event sources for 10 yr of data taking with the same energy-dependent fiducial volume cuts as in Abusleme et al. (2021a) are illustrated. The *y*-axis represents the number of events per 0.1 MeV. The blue and green curves represent singles from the ν_x+^{13}C NC and $\nu_x + e$ ES channels, respectively. The purple curve includes the ν_e +^{13} C $\rightarrow e^-$ +^{13} N($\frac{3}{2}^-$) channel and the residual singles of the ν_e +^{13} C $\rightarrow e^-$ +^{13} N($\frac{1}{2}^-$) channel after the coincidence cut. The red curve represents the single events from natural radioactivity and muon-induced unstable isotopes. The brown curve includes the $\bar{\nu}_e + e$ ES and $\bar{\nu}_x$ +^{13} C NC channels from reactor antineutrinos. The black curve represents the summation of all the components. The upper right insert plot is illustrated for the energy range between 3 and 5 MeV in the linear scale. Note that the discontinuities at 3 and 5 MeV are due to the changes in the fiducial volume size.

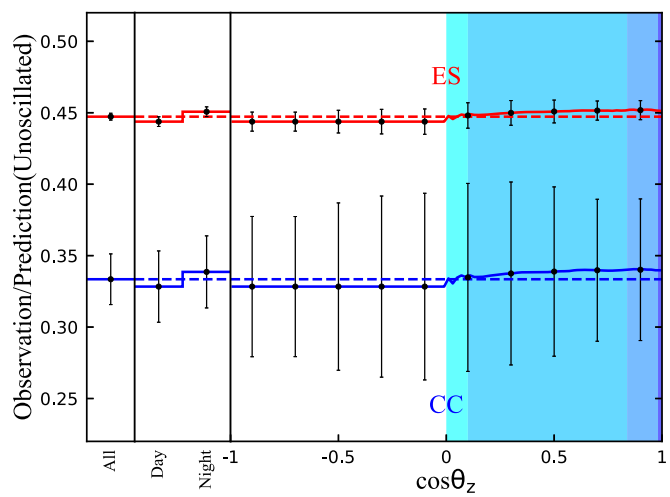

Figure 3. Ratios of the solar neutrino signal event rates with and without considering terrestrial matter effects as the function of the zenith angle for the ES (red solid line) and CC (blue solid line) channels. The dashed lines represent the average over the whole zenith angle range. The ratios for the daytime, nighttime, and day–night average are also shown for comparison. The blue shaded regions with different colors from left to right are used to denote the zenith angle ranges passing through the crust, mantle, and core of Earth. Note that the signal rate in the night is higher than that in the day, due to the ν_e regeneration through Earth.

2.3. ν_x + e ES Channel

In this work, we follow the exact same strategy as in Abusleme et al. (2021a) for the analysis of the $\nu_x + e$ ES channel, where energy spectra for the recoiled electrons as well as all the backgrounds have been shown in Figure 2. One should note that the upturn feature of the energy dependence of the solar neutrino survival probability is clearly visible in the electron energy spectrum.

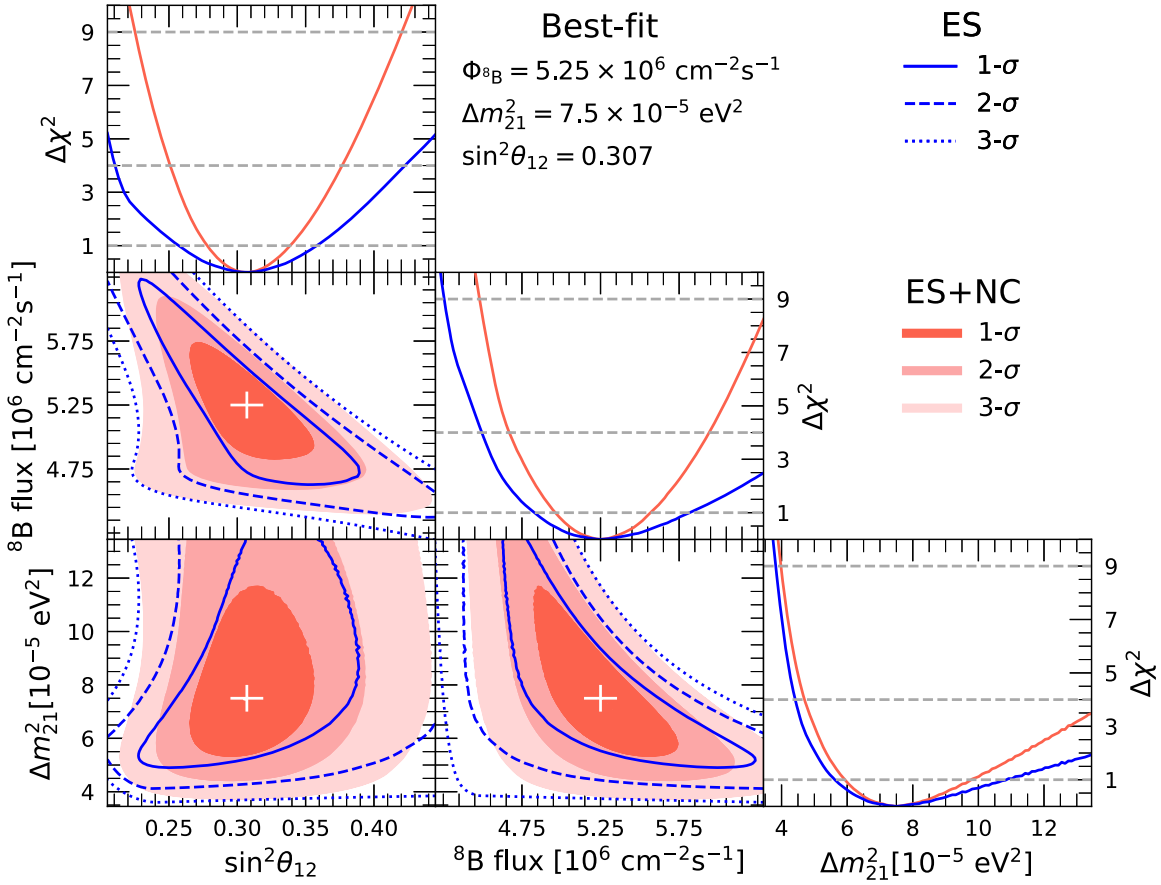

Figure 4. Comparison of the sensitivity on the ^{8}B solar neutrino flux, $\sin^2\theta_{12}$ and Δm^2_{21}, between the ES measurement (single events outside [3.5, 4.1] MeV) and the ES+NC measurement (all singles events). The 1σ (68.3%), 2σ (95.5%), and 3σ (99.7%) allowed regions are illustrated with blue lines and red shaded regions, respectively. The marginalized projections of these parameters are also shown.

2.4. Day–Night Asymmetry

The MSW effect can cause solar neutrino event rate variations as a function of the solar zenith angle when the neutrinos propagate through Earth (Carlson 1986; Baltz & Weneser 1987, 1988; Krastev & Petcov 1988; Akhmedov et al. 2004; Blennow et al. 2004; de Holanda et al. 2004; Liao 2008; Long et al. 2013), and result in the day–night asymmetry of the solar neutrino observation, in which the signal rate in the night is higher than that in the day, due to ν_e regeneration inside Earth.

In this work, in addition to the visible energy spectra of the CC, NC, and ES channels, we also consider the day–night asymmetry to constrain the neutrino oscillation parameters. The location of JUNO (i.e., 112°31′05″ E and 22°07′05″ N (Abusleme et al. 2022a)) is used in the day–night asymmetry calculations, and the two-dimensional visible energy and zenith angle spectra are employed. For illustration, we show in Figure 3 the ratios of solar neutrino signal event rates with and without considering the terrestrial matter effects as the function of the zenith angle θ_z. The red and blue solid lines denote the ES and CC channels, respectively. In comparison, the dashed lines denote the respective averages over the whole zenith angle range. The ratios of the day–night average (R_A), daytime (R_D), and nighttime (R_N) are also illustrated in the first three bins. The error bars are quoted as the statistical uncertainties of the signal and backgrounds. The blue shaded regions with different colors from left to right are used to denote the zenith angle ranges passing through the crust, mantle, and core of Earth, respectively. The day–night asymmetry, defined as $(R_D - R_N)/R_A$, is predicted to be −3.1% and −1.6% for the CC and ES channels respectively. The energy ranges of the CC and ES channels are [5, 14] MeV and [2, 16] MeV, respectively. Given that all the neutrino flavors can be detected through the NC channel, no day–night asymmetry exists in the NC detection. Note that the magnitude of the day–night asymmetry strongly depends on the value of Δm^2_{21}. If Δm^2_{21} is decreased from the KamLAND measurement 7.5×10^{-5} eV^2 (Gando et al. 2013) to 6.1×10^{-5} eV^2 of the global solar neutrino data (Esteban et al. 2020), the absolute values of the day–night asymmetry also increase to −4.2% and −2.2% for the CC and ES channels, respectively.

3. Sensitivity Study

In this section, we study the physical potential for the model-independent measurement of ^{8}B solar neutrinos using the CC, NC, and ES channels. Based on the typical event signatures, the full solar neutrino data can be separated into correlated and single event data sets. As discussed in the previous section, all three interaction channels from ^{8}B solar neutrinos contribute to the single event data set, while the correlated data set includes events from both the CC channel and the accidental coincidence of the ES channel.

In this analysis, we consider the following systematic uncertainties. First, the uncertainty of detection efficiency is

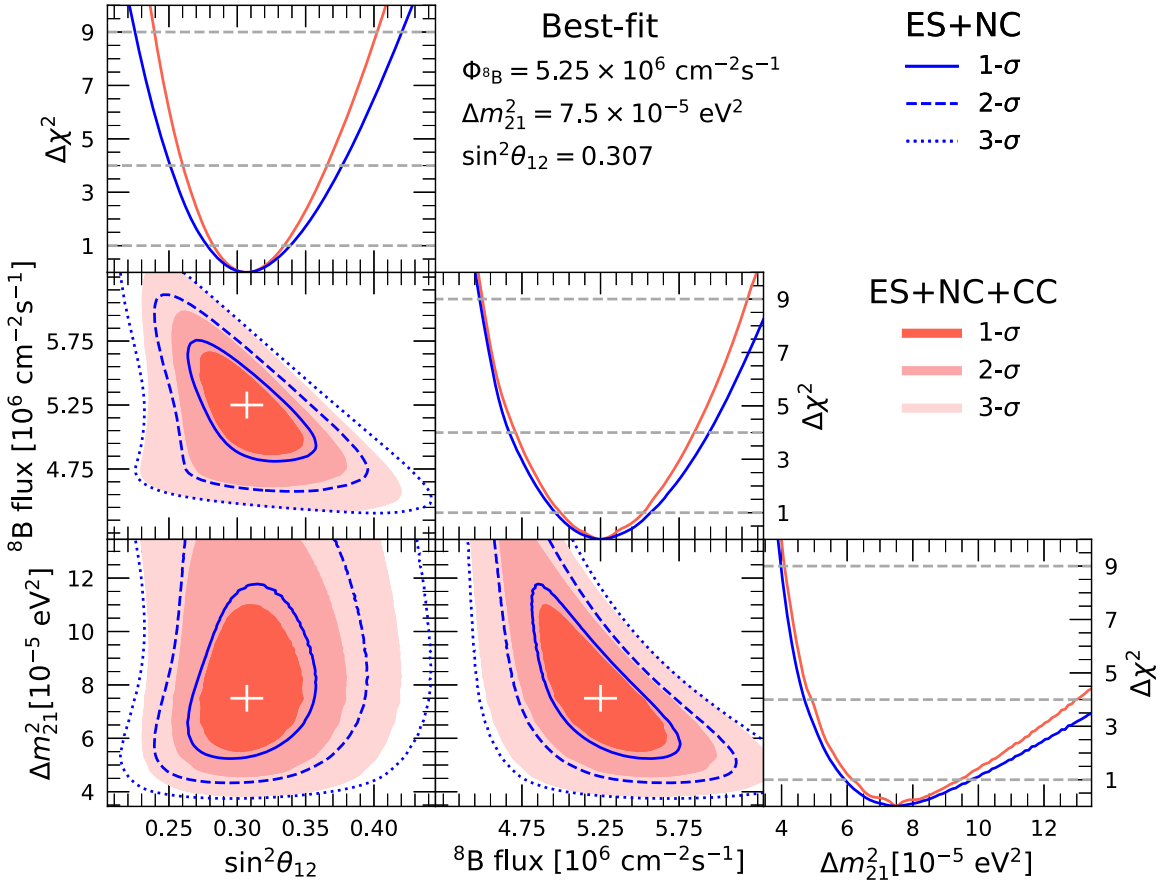

Figure 5. Same as Figure 4, but for the comparison between the ES+NC measurement (all single events) and the ES+NC+CC measurement (both the single events and correlated events).

estimated to be 2% (Abusleme et al. 2021a), which is fully correlated with the the signal and background components of each data set, but uncorrelated between the coincidence and single event data samples. Second, the current uncertainty of the ^{13}C cross sections from the model calculation is at the level of several percent (Fukugita et al. 1988; Suzuki et al. 2012, 2019), but the precision could be reduced to 1% or better with large-scale modern shell-model calculations (Barrett et al. 2013). Therefore, the uncertainties for the ^{13}C CC and NC interaction are taken as 1% for the current study. A 0.5% cross-section uncertainty is used for the ES channel (Tomalak & Hill 2020). Third, the shape of the uncertainty of ^{8}B solar neutrinos is taken from Bahcall et al. (1996) and Bahcall (1997), and the uncertainties for the radioactive and muon-induced backgrounds are the same as those in Abusleme et al. (2021a), namely, 1% for ^{238}U, ^{232}Th, and ^{12}B decays, 3% for ^{8}Li and ^{6}He decays, and 10% for ^{10}C and ^{11}Be decays. A 2% uncertainty is used for the single event from the reactor antineutrino ES interaction. In this work, we treat the ^{8}B solar neutrino flux as a free parameter since we are performing a model-independent measurement. Only in the scenario of combining with the SNO flux measurement, an uncertainty of 3.8% is used as an informative prior.

The standard Poisson-type χ^2 method using the Asimov data set (Zyla et al. 2020) is employed to estimate the sensitivity to measure the ^{8}B solar neutrino flux and the oscillation parameters $\sin^2\theta_{12}$ and Δm^2_{21}, where different pull parameters are included in the χ^2 function to account for the systematic uncertainties described in this section. More technical details on the construction of the χ^2 function are provided in the Appendix. In order to identify the contribution of each interaction channel, we divide the whole data sets into the correlated events, the single events within [3.5, 4.1] MeV, and the single events outside [3.5, 4.1] MeV, which correspond to the CC, NC, and ES measurements respectively.

In Figures 4–6, we illustrate the two-dimensional allowed ranges and the marginalized one-dimensional curves on the sensitivity of the ^{8}B neutrino flux, $\sin^2\theta_{12}$ and Δm^2_{21}, of which Figure 4 shows the comparison of the ES and ES+NC measurements, Figure 5 for the comparison the ES+NC and ES +NC+CC measurements, and Figure 6 for the comparison of the JUNO and JUNO + SNO flux measurements. In addition, a summary of relative uncertainties on the ^{8}B neutrino flux, $\sin^2\theta_{12}$ and Δm^2_{21}, from the model-independent approach is provided in Figure 7. Several important observations and comments are presented as follows.

1. The NC measurement is accomplished based on the single events within [3.5, 4.1] MeV, where the background events are from the singles of ES and CC interactions of ^{8}B solar neutrinos, together with the natural radioactivity and muon-induced unstable isotopes. The standard MSW effect of solar neutrino oscillations is used in the calculation of ES and CC interactions and the oscillation parameters $\sin^2\theta_{12}$ and Δm^2_{21} are marginalized. The ^{8}B solar neutrino flux can be obtained with an accuracy of 10.6% with the NC measurement, which is

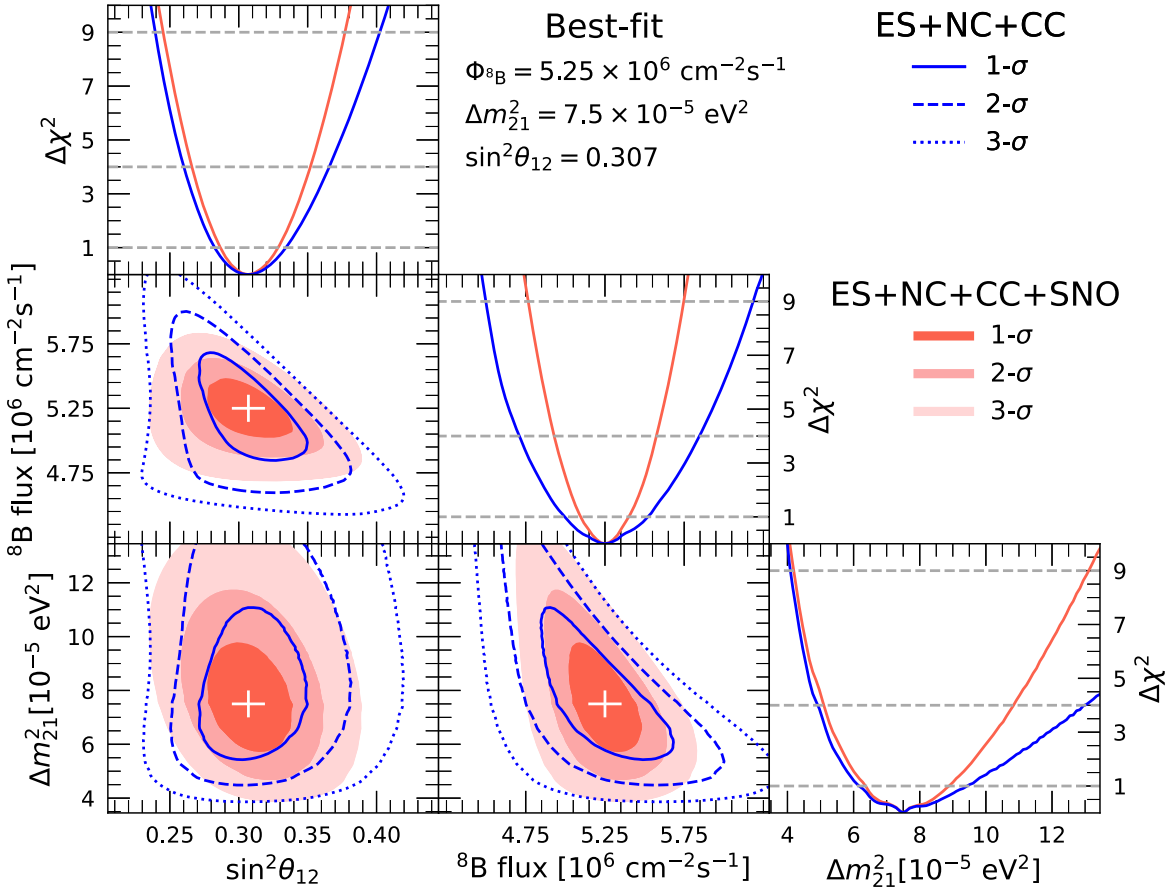

Figure 6. Same as Figure 4, but for the comparison between the ES+NC+CC measurement from JUNO and the combined JUNO+SNO flux measurement.

comparable to the level of 8.6% from the NC measurement of the SNO Phase III data (Aharmim et al. 2013a).

2. The ES measurement is based on the single events outside the energy range of [3.5, 4.1] MeV, in which the dominant background is from the natural radioactivity and muon-induced unstable isotopes, which are summarized in Figure 2 and more details can be found in Abusleme et al. (2021a). In the model-independent approach of the ES measurement, the ^{8}B neutrino flux and two oscillation parameters, $\sin^2\theta_{12}$ and Δm^2_{21}, are simultaneously constrained, where the relative uncertainties are derived as $^{+11\%}_{-8\%}$, $^{+17\%}_{-17\%}$, and $^{+45\%}_{-25\%}$, respectively. The uncertainties of $\sin^2\theta_{12}$ and Δm^2_{21} are larger than those obtained in Abusleme et al. (2021a) by including the 3.8% SNO flux measurement because of the strong correlation between the flux and oscillation parameters in the model-independent approach. When adding the JUNO NC measurement, the accuracy of the ^{8}B neutrino flux can be improved to the level of $^{+6.0\%}_{-5.5\%}$, and the uncertainties of $\sin^2\theta_{12}$ and Δm^2_{21} are also improved to $^{+10\%}_{-10\%}$, and $^{+31\%}_{-21\%}$, respectively.
3. The CC measurement with the correlated events alone cannot simultaneously determine the ^{8}B neutrino flux and oscillation parameters because of the high visible energy threshold. However, combining the CC measurement with the single events of the NC+ES channels will help break the correlation and possible degeneracy among different parameters, where the accuracy of the ^{8}B neutrino flux can be further improved to 5%, while those of $\sin^2\theta_{12}$ and Δm^2_{21} are $^{+9\%}_{-8\%}$, and $^{+25\%}_{-17\%}$, respectively.
4. The expected 5% precision of the ^{8}B neutrino flux obtained with all three detection channels is much better than that of 11.6% from the latest prediction of the SSM (Vinyoles et al. 2017). This will be the only model-independent measurement after those of SNO (Aharmim et al. 2013b). In addition, the uncertainties of $\sin^2\theta_{12}$ and Δm^2_{21} from the ^{8}B neutrino measurement at JUNO are at the levels of $^{+9\%}_{-8\%}$ and $^{+25\%}_{-17\%}$, respectively, which is comparable to the levels of $^{+5\%}_{-5\%}$, and $^{+20\%}_{-11\%}$ from the latest results of combined SK and SNO solar neutrino data (Super-Kamiokande Collaboration et al. 2023). Considering that the reactor antineutrino measurement from JUNO will obtain sub-percent levels of $\sin^2\theta_{12}$ and Δm^2_{21} in the near future (Abusleme et al. 2022b), measurements of these parameters from future solar neutrino data would be important to test the charge, parity, and time reversal symmetry of fundamental physics and resolve the possible discrepancy between the neutrino and antineutrino oscillation channels.
5. Within the spirit of the model-independent approach, one can also include the 3.8% ^{8}B neutrino flux measurement from SNO as an informative prior, where even better precision levels of the flux and oscillation parameters can be achieved. In this scenario, the expected accuracy of the ^{8}B solar neutrino flux would reach the level of 3%, and $\sin^2\theta_{12}$ and Δm^2_{21} can be constrained with the precision of

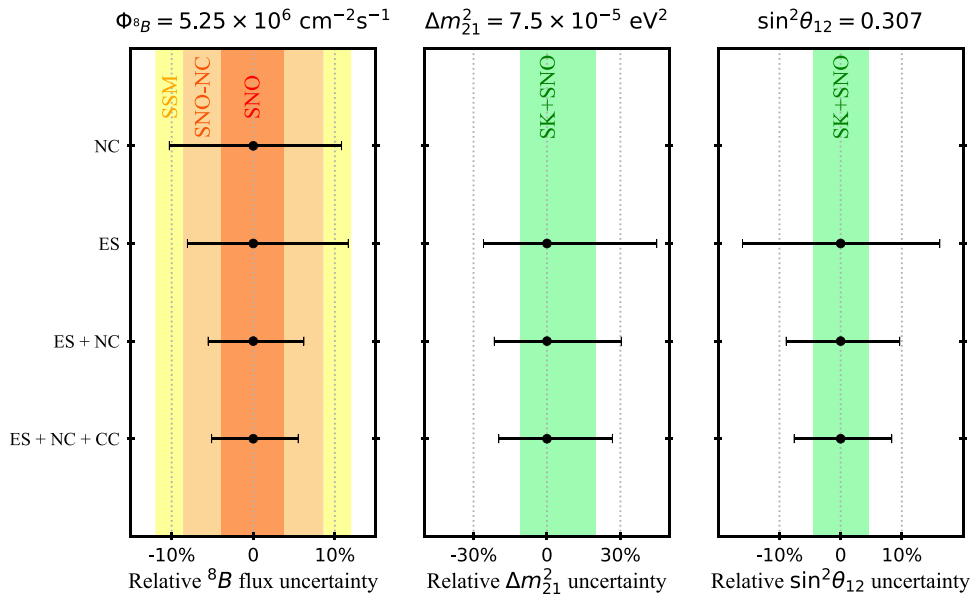

Figure 7. Relative uncertainties of the ^{8}B solar neutrino flux (left panel), Δm^2_{21} (middle panel), and $\sin^2\theta_{12}$ (right panel) from the model-independent approach with different combinations of the data sets. The colored bands in the left panel represent the flux uncertainty from the SSM data (Vinyoles et al. 2017), the NC measurement of the SNO Phase III data (SNO-NC) (Aharmim et al. 2013a), and the combined SNO CC, NC, and ES data (SNO) (Aharmim et al. 2013b). The green bands in the middle and right panels represent the uncertainty of oscillation parameters from the combined SK and SNO solar neutrino data (Super-Kamiokande Collaboration et al. 2023).

$^{+7.5\%}_{-6.5\%}$, and $^{+19\%}_{-15\%}$, respectively. These measurements are comparable to those from the current global solar neutrino data and would provide unique information to the future solar neutrino program.

6. It is noteworthy that the signal event statistics, detection efficiency, and cross-section uncertainties are the most crucial factors that affect the detection potential of the CC and NC detection channels. If the cross-section uncertainties are 10%, instead of 1% assumed in this work, the uncertainty of the ^{8}B neutrino flux will become $^{+6\%}_{-6\%}$.
7. In the CC detection channel, the observed energy of the prompt electron is directly related to the incoming neutrino energy, making it crucial to lower the prompt energy threshold to investigate the predicted increase in the solar neutrino survival probability at lower energies. For this analysis, we set a conservative prompt energy threshold at 5 MeV to optimize the trade-off between signal detection efficiencies and background contamination. Regarding the accidental background, radioactivity is the primary source of the prompt signal below 3.5 MeV, where stringent background control measures are essential, as outlined in Abusleme et al. (2021b). Conversely, solar neutrino ES events become the leading prompt signal above 3.5 MeV. For the prompt energy range of 3.5–5 MeV, the cosmogenic correlated background is significantly higher than in the region above 5 MeV, as depicted in Figure 1, while the signal efficiency is considerably lower between 3.5 and 5 MeV, due to the multiplicity cut. Additional technical details in this regard will be reported elsewhere in the future.

4. Concluding Remarks

In this work, we have studied the physics potential of detecting ^{8}B solar neutrinos at JUNO, in a model-independent manner by using the CC, NC, and ES detection channels. Because of its largest-ever mass of ^{13}C and the expected low background level, excellent signal-to-background ratios can be achieved. Thus, ^{8}B solar neutrinos will be observable in all three interaction channels.

We have performed detailed evaluations of the background budgets and signal efficiencies of the CC, NC, and ES channels at JUNO. With optimized selection strategies, we find that the expected ^{8}B neutrino rates of the CC and NC channels are $\mathcal{O}(100)$ interactions per year after the event selection. It turns out that the signal event statistics, detection efficiency, and cross-section uncertainties are the most crucial factors that affect the detection potential of these two channels. We have carried out a combined analysis of both the coincidence and single events from all three detection channels, and shown that the ^{8}B solar neutrino flux, $\sin^2\theta_{12}$ and Δm^2_{21}, can be measured to $\pm 5\%$, $^{+9\%}_{-8\%}$, and $^{+25\%}_{-17\%}$, respectively. When combined with the SNO flux measurement, the world's best precision of 3% can be achieved for the ^{8}B neutrino flux.

In the history of solar neutrino experiments, the NC measurement is unique in decoupling the neutrino flux and oscillation parameters, and enabling the model-independent approach of the solar neutrino program. SNO has been the only solar neutrino experiment in the past to achieve this goal, and JUNO would be the second one. In this work, we have demonstrated the feasibility of ^{8}B solar neutrino measurements at JUNO, which, together with other large solar neutrino detectors (Beacom et al. 2017; Abe et al. 2018; Capozzi et al. 2019), will open a new era of solar neutrino observation and may uncover new directions for neutrino physics and solar physics.

Acknowledgments

We are grateful for the ongoing cooperation from the China General Nuclear Power Group. This work was supported by the Chinese Academy of Sciences, the National Key R&D

Program of China, the CAS Center for Excellence in Particle Physics, Wuyi University, and the Tsung-Dao Lee Institute of Shanghai Jiao Tong University in China, the Institut National de Physique Nucléaire et de Physique de Particules (IN2P3) in France, the Istituto Nazionale di Fisica Nucleare (INFN) in Italy, the Italian-Chinese collaborative research program MAECI-NSFC, the Fond de la Recherche Scientifique (F.R.S-FNRS) and FWO under the "Excellence of Science—EOS" in Belgium, the Conselho Nacional de Desenvolvimento Científico e Tecnològico in Brazil, the Agencia Nacional de Investigacion y Desarrollo and ANID—Millennium Science Initiative Program—ICN2019_044 in Chile, the Charles University Research Center and the Ministry of Education, Youth, and Sports in Czech Republic, the Deutsche Forschungsgemeinschaft (DFG), the Helmholtz Association, and the Cluster of Excellence PRISMA+ in Germany, the Joint Institute of Nuclear Research (JINR) and Lomonosov Moscow State University in Russia, the joint Russian Science Foundation (RSF) and National Natural Science Foundation of China (NSFC) research program, the MOST and MOE in Taiwan, the Chulalongkorn University and Suranaree University of Technology in Thailand, University of California at Irvine, and the National Science Foundation in the US.

Appendix

In this appendix, we present the technical details of the sensitivity study employed in this work. A Poisson-type least squares function, denoted as χ^2, is defined as follows:

$$\begin{aligned}\chi^2 &= \chi^2_{\rm stat}({\rm CC}) + \chi^2_{\rm stat}({\rm NC}) + \chi^2_{\rm stat}({\rm ES}) + \chi^2_{\rm syst}\\ &= 2\times\sum_{i=1}^{10}\Bigg[\sum_{j_{\rm C}=1}^{90}\left(N^{\rm C}_{\rm pre}(\theta^i_z, E^{j_{\rm C}}_{\rm vis}) - N^{\rm C}_{\rm obs}(\theta^i_z, E^{j_{\rm C}}_{\rm vis}) + N^{\rm C}_{\rm obs}(\theta^i_z, E^{j_{\rm C}}_{\rm vis})\cdot\log\frac{N^{\rm C}_{\rm obs}(\theta^i_z, E^{j_{\rm C}}_{\rm vis})}{N^{\rm C}_{\rm pre}(\theta^i_z, E^{j_{\rm C}}_{\rm vis})}\right)\\ &\quad+\sum_{j_{\rm S}=1}^{140}\left(N^{\rm S}_{\rm pre}(\theta^i_z, E^{j_{\rm S}}_{\rm vis}) - N^{\rm S}_{\rm obs}(\theta^i_z, E^{j_{\rm S}}_{\rm vis}) + N^{\rm S}_{\rm obs}(\theta^i_z, E^{j_{\rm S}}_{\rm vis})\cdot\log\frac{N^{\rm S}_{\rm obs}(\theta^i_z, E^{j_{\rm S}}_{\rm vis})}{N^{\rm S}_{\rm pre}(\theta^i_z, E^{j_{\rm S}}_{\rm vis})}\right)\Bigg]\\ &\quad+\left(\frac{\varepsilon^{\rm ES}_X}{\sigma^{\rm ES}_X}\right)^2+\left(\frac{\varepsilon^{\rm NC}_X}{\sigma^{\rm NC}_X}\right)^2+\left(\frac{\varepsilon^{\rm CC}_X}{\sigma^{\rm CC}_X}\right)^2+\sum_{k_{\rm C}}\left(\frac{\varepsilon^{k_{\rm C}}_{\rm B}}{\sigma^{k_{\rm C}}_{\rm B}}\right)^2+\sum_{k_{\rm S}}\left(\frac{\varepsilon^{k_{\rm S}}_{\rm B}}{\sigma^{k_{\rm S}}_{\rm B}}\right)^2\\ &\quad+\left(\frac{\varepsilon^{\rm C}_{\rm eff}}{\sigma^{\rm C}_{\rm eff}}\right)^2+\left(\frac{\varepsilon^{\rm S}_{\rm eff}}{\sigma^{\rm S}_{\rm eff}}\right)^2+(\varepsilon_{\rm s})^2,\end{aligned}\tag{A1}$$

where $\chi^2_{\rm stat}({\rm CC})$, $\chi^2_{\rm stat}({\rm NC})$, and $\chi^2_{\rm stat}({\rm ES})$ are statistical parts of the CC, NC, and ES channels in the χ^2 function, respectively. These components are presented in the second and third rows of Equation (A1). The index $j_{\rm C}$ ranges from 1–90 for the CC measurement, representing the energy range from 5–14 MeV with an equal bin width of 0.1 MeV. For the NC measurement, $j_{\rm S}$ ranges from 16–21, while for the ES measurement, $j_{\rm S}$ spans from 1–15 and 22–140 covering the energy range of 2–16 MeV with an equal bin width of 0.1 MeV. The predicted numbers of signal and background events, $N^{\rm C}_{\rm pre}(\theta^i_z, E^{j_{\rm C}}_{\rm vis})$ and $N^{\rm S}_{\rm pre}(\theta^i_z, E^{j_{\rm S}}_{\rm vis})$, are calculated for the ith zenith angle bin and the $j_{\rm C}$th or $j_{\rm S}$th visible energy bin of the correlated and single event samples, respectively,

$$\begin{aligned}N^{\rm C}_{\rm pre}(\theta^i_z, E^{j_{\rm C}}_{\rm vis} &= (1+\varepsilon^{\rm C}_{\rm eff})S^{\rm CC}_{\rm pre}(\theta^i_z, E^{j_{\rm C}}_{\rm vis})\\ &\quad+\sum_{k_{\rm C}}(1+\varepsilon^{k_{\rm C}}_{\rm B})B^{k_{\rm C}}_{\rm pre}(\theta^i_z, E^{j_{\rm C}}_{\rm vis}),\end{aligned}\tag{A2}$$

$$\begin{aligned}N^{\rm S}_{\rm pre}(\theta^i_z, E^{j_{\rm S}}_{\rm vis}) &= (1+\varepsilon^{\rm S}_{\rm eff})[S^{\rm NC}_{\rm pre}(\theta^i_z, E^{j_{\rm C}}_{\rm vis})\\ &\quad+S^{\rm ES}_{\rm pre}(\theta^i_z, E^{j_{\rm C}}_{\rm vis})]\\ &\quad+\sum_{k_{\rm S}}(1+\varepsilon^{k_{\rm S}}_{\rm B})B^{k_{\rm S}}_{\rm pre}(\theta^i_z, E^{j_{\rm S}}_{\rm vis}),\end{aligned}\tag{A3}$$

where $S^{\rm CC}_{\rm pre}$, $S^{\rm NC}_{\rm pre}$, and $S^{\rm ES}_{\rm pre}$ represent the two-dimensional spectra of the ^{8}B neutrino signals in the CC, NC, and ES channels, respectively, incorporating the fiducial volume and signal efficiencies. The projections of these spectra onto the visible energy axis are depicted in Figure 1 for the CC channel and Figure 2 for the NC and ES channels. Meanwhile, $B^{k_{\rm C}}_{\rm pre}$ and $B^{k_{\rm S}}_{\rm pre}$ correspond to the background components in the correlated and single event samples, respectively, with their visible energy spectra illustrated in the same figures. The calculations of the ^{8}B neutrino signal spectra in the CC, NC, and ES channels are as follows:

$$\begin{aligned}S^{\rm CC}_{\rm pre}(\theta^i_z, E^{j_{\rm C}}_{\rm vis}) &= \Phi_{^8{\rm B}}\times\Big[(1+\varepsilon_{\rm s}\delta^{\rm S}_{E_\nu})S_{^8{\rm B}}(E_\nu)\\ &\quad\times P_{ee}(\theta_{12}, \Delta m^2_{21}, E_\nu, \theta^i_z)\\ &\quad\times(1+\varepsilon^{\rm CC}_X)\otimes\sigma_{\rm CC}(E_\nu, E_e)\otimes M(E_e, E^{j_{\rm C}}_{\rm vis})\Big],\end{aligned}\tag{A4}$$

$$\begin{aligned}S^{\rm NC}_{\rm pre}(\theta^i_z, E^{j_{\rm C}}_{\rm vis}) &= \Phi_{^8{\rm B}}\times\Big[(1+\varepsilon_{\rm s}\delta^{\rm S}_{E_\nu})S_{^8{\rm B}}(E_\nu)\\ &\quad\times(1+\varepsilon^{\rm NC}_X)\otimes\sigma_{\rm NC}(E_\nu, E_\gamma)\otimes M(E_\gamma, E^{j_{\rm S}}_{\rm vis})\Big],\end{aligned}\tag{A5}$$

Table 3
Description of the Nuisance Parameters and the Associated Uncertainties in the χ^2 Function

Sys.	Description of the Pull Term	Uncertainty
$\varepsilon_X^{\rm ES}$, $\varepsilon_X^{\rm NC}$, $\varepsilon_X^{\rm CC}$	Cross section for the CC, NC, and ES channels	1%, 1%, 0.5%
$\varepsilon_{\rm eff}^{\rm C}$, $\varepsilon_{\rm eff}^{\rm S}$	Detector efficiency	2% (Abusleme et al. 2021a)
$\varepsilon_{\rm B}^{k_{\rm C}}$, $\varepsilon_{\rm B}^{k_{\rm S}}$	Rate for the $k_{\rm C}$th or $k_{\rm S}$th background component	1%–10%, same as Abusleme et al. (2021a)
$\varepsilon_{\rm s}$	^{8}B neutrino energy spectrum	Bahcall et al. (1996), Bahcall (1997)

$$S_{\rm pre}^{\rm ES}(\theta_z^i, E_{\rm vis}^{j_{\rm C}}) = \Phi_{^8{\rm B}} \times \Big\{(1+\varepsilon_{\rm s}\delta_{E_\nu}^{\rm S})S_{^8{\rm B}}(E_\nu) \times \Sigma_\alpha\Big[P_{e\alpha}(\theta_{12}, \Delta m_{21}^2, E_\nu, \theta_z^i) \times (1+\varepsilon_X^{\rm ES}) \otimes \sigma_{\rm ES}^{\nu_\alpha}(E_\nu, E_e)\Big] \otimes M(E_e, E_{\rm vis}^{j_{\rm C}})\Big\}. \tag{A6}$$

The ^{8}B neutrino signal spectra for the CC, NC, and ES channels are calculated by multiplying the ^{8}B neutrino spectrum $S_{^8{\rm B}}$ with the neutrino oscillation probability $P_{e\alpha}$ (where α equals e or $\mu+\tau$), and then convolving the resulting product with the differential interaction cross sections (namely, $\sigma_{\rm CC}$, $\sigma_{\rm NC}$, and $\sigma_{\rm ES}^{\nu_\alpha}$) as well as with the detector response matrix M. The neutrino oscillation probability $P_{e\alpha}$ includes both the standard MSW flavor conversion and terrestrial matter effects, and is a function of the neutrino energy E_ν and the zenith angle θ_z, calculated within the three-neutrino oscillation framework. The detector response matrix M accounts for the effects of energy resolution and energy nonlinearity, as described in Abusleme et al. (2021a). The observed spectra $N_{\rm obs}^{\rm C}(\theta_z^i, E_{\rm vis}^{j_{\rm C}})$ and $N_{\rm obs}^{\rm S}(\theta_z^i, E_{\rm vis}^{j_{\rm S}})$ are obtained from the corresponding predicted spectra by applying the true values of the ^{8}B neutrino flux $\Phi_{^8{\rm B}}$, oscillation parameters $\sin^2\theta_{12}$, and Δm_{21}^2, and assuming negligible contributions from nuisance parameters. Note that, as discussed in Section 2, the ^{8}B solar neutrino interactions may also contribute to the background components $B_{\rm pre}^{k_{\rm C}}$ (e.g., the green line in Figure 1, the purple line in Figure 2), In such instances, all correlations between the signal and background components are accounted for in the χ^2 function.

The nuisance parameters ε_X^m (m = CC, NC, ES), $\varepsilon_{\rm B}^k$, $\varepsilon_{\rm eff}^n$ (n = C, S) account for systematic uncertainties associated with the cross section, the backgrounds, and the detection efficiency, respectively, as discussed in the manuscript. The parameter $\delta_{E_\nu}^{\rm S}$ represents the 1σ fractional variation of the ^{8}B neutrino energy spectrum, as detailed in Bahcall et al. (1996) and Bahcall (1997), while $\varepsilon_{\rm s}$ denotes the magnitude of the ^{8}B neutrino spectral uncertainty. A summary of the nuisance parameters and their corresponding uncertainties within the χ^2 function is summarized in Table 3. For the sensitivity study that produced the results shown in Figures 4–7, we selected data sets from one or a combination of the CC, NC, and ES measurements. We then activated the relevant nuisance parameters to account for systematic uncertainties in the corresponding χ^2 function. During the calculation of the allowed regions for each analysis, the displayed parameters (one or two of the fitting parameters $\Phi_{^8{\rm B}}$, θ_{12}, and Δm_{21}^2) were fitted, while all other physical and nuisance parameters were marginalized. The critical values of $\Delta\chi^2$ for various confidence levels are sourced from Zyla et al. (2020).

References

Abazov, A. I., Anosov, O. L., Faizov, E. L., et al. 1991, PhRvL, 67, 3332
Abe, K., Haga, Y., Hayato, Y., et al. 2016, PhRvD, 94, 052010
Abe, K., Abe, Ke., Aihara, H., et al. 2018, arXiv:1805.04163
Abusleme, A., Adam, T., Ahmad, S., et al. 2021a, ChPhC, 45, 023004
Abusleme, A., Adam, T., Ahmad, S., et al. 2021b, JHEP, 11, 102
Abusleme, A., Adam, T., Ahmad, S., et al. 2022a, PrPNP, 123, 103927
Abusleme, A., Adam, T., Ahmad, S., et al. 2022b, ChPhC, 46, 123001
Agostini, M., Altenmüller, K., Appel, S., et al. 2020, Natur, 587, 577
Aharmim, B., Ahmed, S. N., Amsbaugh, J. F., et al. 2008, PhRvL, 101, 111301
Aharmim, B., Ahmed, S. N., Amsbaugh, J. F., et al. 2013a, PhRvC, 87, 015502
Aharmim, B., Ahmed, S. N., Anthony, A. E., et al. 2013b, PhRvC, 88, 025501
Ahmad, Q. R., Allen, R. C., Andersen, T. C., et al. 2001, PhRvL, 87, 071301
Ahmad, Q. R., Allen, R. C., Andersen, T. C., et al. 2002, PhRvL, 89, 011301
Ahmed, S., Anthony, A. E., Beier, E. W., et al. 2004, PhRvL, 92, 181301
Akhmedov, E. K., Tortola, M. A., & Valle, J. W. F. 2004, JHEP, 05, 057
Altmann, M., Balata, M., Belli, P., et al. 2000, PhLB, 490, 16
Anselmann, P., Hampel, W., Heusser, G., et al. 1993, NuPhS, 31, 117
Arafune, J., Fukugita, M., Kohyama, Y., & Kubodera, K. 1989, PhLB, 217, 186
Bahcall, J. N. 1997, PhRvC, 56, 3391
Bahcall, J. N., Lisi, E., Alburger, D. E., et al. 1996, PhRvC, 54, 411
Baltz, A. J., & Weneser, J. 1987, PhRvD, 35, 528
Baltz, A. J., & Weneser, J. 1988, PhRvD, 37, 3364
Barrett, B. R., Navratil, P., & Vary, J. P. 2013, PrPNP, 69, 131
Beacom, J. F., Chen, S., Cheng, J., et al. 2017, ChPhC, 41, 023002
Bellini, G., Benziger, J., Bick, D., et al. 2014, Natur, 512, 383
Blennow, M., Ohlsson, T., & Snellman, H. 2004, PhRvD, 69, 073006
Buldgen, G., Eggenberger, P., Noels, A., et al. 2023, A&A, 669, L9
Capozzi, F., Li, S. W., Zhu, G., & Beacom, J. F. 2019, PhRvL, 123, 131803
Carlson, E. D. 1986, PhRvD, 34, 1454
Chen, H. H. 1985, PhRvL, 55, 1534
Davis, R., Jr., Harmer, D. S., & Hoffman, K. C. 1968, PhRvL, 20, 1205
de Holanda, P. C., Liao, W., & Smirnov, A. Y. 2004, NuPhB, 702, 307
Esteban, I., Gonzalez-Garcia, M. C., Maltoni, M., Schwetz, T., & Zhou, A. 2020, JHEP, 09, 178
Fukuda, S., Fukuda, Y., Ishitsuka, M., et al. 2001, PhRvL, 86, 5651
Fukuda, Y., Hayakawa, T., Ichihara, E., et al. 1998, PhRvL, 81, 1158
Fukugita, M., Kohyama, Y., & Kubodera, K. 1988, PhLB, 212, 139
Gando, A., Gando, Y., Hanakago, H., et al. 2013, PhRvD, 88, 033001
Ghiano, C. 2012, PhD thesis, L'Aquila Univ.
Hirata, K. S., Kajita, T., Kifune, T., et al. 1989, PhRvL, 63, 16
Ianni, A., Montanino, D., & Villante, F. L. 2005, PhLB, 627, 38
Krastev, P. I., & Petcov, S. T. 1988, PhLB, 205, 84
Liao, W. 2008, PhRvD, 77, 053002
Lin, T., Zou, J., Li, W., et al. 2017, JPhCS, 898, 042029
Long, H. W., Li, Y. F., & Giunti, C. 2013, JHEP, 08, 056
Magg, E., Bergemann, M., Serenelli, A., et al. 2022, A&A, 661, A140
Mikheev, S. P., & Smirnov, A. Y. 1985, SvJNP, 42, 913
Super-Kamiokande Collaboration, Abe, K., Bronner, C., et al. 2023, arXiv:2312.12907
Renshaw, A., Abe, K., Iyogi, K., et al. 2014, PhRvL, 112, 091805
Suzuki, T., Balantekin, A. B., Kajino, T., & Chiba, S. 2019, JPhG, 46, 075103
Suzuki, T., Balantekin, A. B., & Kajino, T. 2012, PhRvC, 86, 015502
Tomalak, O., & Hill, R. J. 2020, PhRvD, 101, 033006
Vinyoles, N., Serenelli, A. M., Villante, F. L., et al. 2017, ApJ, 835, 202
Wolfenstein, L. 1978, PhRvD, 17, 2369
Yang, W. 2022, ApJ, 939, 61
Zou, J. H., Huang, X. T., Li, W. D., et al. 2015, JPhCS, 664, 072053
Zyla, P. A., Barnett, R. M., Beringer, J., et al. 2020, PTEP, 2020, 083C01